The Fluid Dynamics of Secondary Cooling Air-Mist Jets

I. HERNÁNDEZ C., F.A. ACOSTA G., A.H. CASTILLEJOS E., and J.I. MINCHACA M.

For the conditions of thin-slab continuous casting, air-mist secondary cooling occurs in the transition-boiling regime, possibly as a result of an enhanced intermittent contact of high-momentum water drops with the hot metallic surface. The dynamics of the intermittent contact or wetting/dewetting process should be primarily dependent on the drop size, drop impact-velocity and -angle and water-impact flux, which results from the nozzle design and the inter-action of the drops with the conveying and entrained air stream. The aim of this article was to develop a model for predicting the last three parameters based on the design and operating characteristics of air-mist nozzles and on experimentally determined drop-size distributions. To do this, the Eulerian fluid-flow field of the air in three dimensions and steady state and the Lagrangian velocities and trajectories of water drops were computed by solving the turbulent Navier–Stokes equation for the air coupled to the motion equation for the water drops. In setting this model, it was particularly important to specify appropriately the air-velocity profile at the nozzle orifice, as well as, the water-flux distribution, and the velocities (magnitude and angle) and exit positions of drops with the different sizes generated, hence special attention was given to these aspects. The computed drop velocities, water-impact flux distributions, and air-mist impact-pressure fields compared well with detailed laboratory measurements carried out at ambient temperature. The results indicate that under practical nozzle-operating conditions, the impinging-droplet Weber numbers are high, over most of the water footprint, suggesting that the droplets should establish an intimate contact with the solid surface. However, the associated high mean-droplet fluxes hint that this contact may be obstructed by drop interference at the surface, which would undermine the heat-extraction effectiveness of the impinging mist. The model also points out that a large proportion of fine drops would be prevented by the air-flow pattern from reaching the surface. The numerical analysis of air-mist jets under conditions relevant to secondary cooling had not been addressed before, and it constitutes a first step in an effort to develop a model to describe the dynamic and thermal interaction of dense-drop media with hot metallic surfaces.

I. INTRODUCTION

AN appropriate secondary cooling system for continuous casting of steel should be able to provide a heat-extraction distribution on the strand surface that grants optimum levels of quality and productivity. If this is not the case, bulging, cracks, segregation, and, ultimately, poor metallurgical quality and operating practice will result. A review of defects linked to spray-cooling practice in billets and slabs was presented by Brimacombe et al.[1] In their excellent article, the authors pointed out that both the intensity and uniformity of the heat removal should be controlled to avoid low ductility and large tensile strains, which are potential sources of quality problems. In continuous casting, air-mist (pneumatic) nozzles are gaining acceptance over hydraulic nozzles owing mainly to two claimed advantages: (a) a more uniform heat extraction and (b) a broader range of heat-removal intensities. It could be suggested that the first arises from the even dispersion of drops that results from the trajectories imparted to them by the nozzle-orifice geometry and the accompanying air, and that the second is a consequence of the wide turndown ratio (ratio between the minimum and maximum water flow) and the controllability of the air/water voluminic-flows ratio, A/W. Recently, the control of this last ratio (at approximately 10) was found to give the possibility of increasing productivity (casting speed) of thin slabs without a detriment on quality and despite that cooling occurs in the transition- boiling regime.[2] In this regime, the heat flux and heat-transfer coefficient are a strong function of surface temperature in contrast to the film-boiling regime that is prevalent and is sought out in the continuous casting of conventional slabs.[3] When the solid-surface superheat (i.e., the difference between the surface temperature and the liquid-saturation temperature) is "sufficient," the film-boiling state is reached, where the liquid drops are not in direct contact with the hot surface but are separated by a continuous film of vapor. Because the superheats in conventional- and thin-slab casting are

I. HERNÁNDEZ C., Doctoral Student, F.A. ACOSTA G., Associate Professor, A.H. CASTILLEJOS E., Professor, and J.I. MINCHACA M., Master of Science Student, are with CINVESTAV – Unidad Saltillo, Carr. Saltillo-Monterrey Km. 13, Saltillo, 25000, Coahuila, México. Contact e-mail: humberto.castillejos@cinvestav.edu.mx

similar, the different boiling behavior of the drops must be associated with the dynamic parameters affecting the chances of drop contact with the surface, *i.e.*, drop size, drop-normal and tangential velocities, and droplet-impact flux. This article presents a study of these parameters for the case of fan air-mist nozzles, which produce flat impact footprints and are widely used in continuous casting of steel.

It has been reported that there is a direct dependency of the heat transfer on the droplet diameter and its initial collision velocity[4,5] and that this is an indication of the important relationship between the heat-transfer process and the droplet-deformation behavior during impact.[6] The Weber number ($We_{zs} = \rho_d u_{zs}^2 d_d / \sigma$) associated with the normal-collision velocity, u_{zs}, has in general been agreed to characterize the impact or deformation mode of the drops.[6,7] From low to high (≥30) We_{zs} numbers, there is a transition from nonwetting to wetting impact for single drops.[7] In the nonwetting mode, the heat extraction occurs in the stable film-boiling regime with the droplet vaporizing during a short contact time, after which it rebounds, and its direct contact is obstructed by the vapor, while in the wetting mode, the droplet does not vaporize instantaneously but spreads and breaks, forming a thin film that causes a high heat transfer.[5] The response of these two regimes to the impinging rate of droplets is quite different, even at very low rates (0.5 to 3 drops/s).[8] In the nonwetting regime, the heat-transfer coefficient is independent of the impinging rate, while in the wetting regime, there is a significant decrease as the impinging frequency increases, apparently because the liquid layer from foregoing droplets hinder the heat transfer of the succeeding droplets, even at these small rates. The impact frequency influences the thickness of the liquid film formed on the solid surface, which in turn affects the dynamic processes taking place when a single drop with high velocity impacts onto a liquid layer.[9]

The effect of the Weber number on the impaction heat transfer has been investigated by Choi and Yao[10] with water sprays involving relatively low-impact water fluxes ($0.11 \leq w \leq 1.84 \, \text{L/m}^2 \, \text{s}$). For the more dilute sprays, they found that the boiling-heat transfer increased with the Weber number, while for the denser sprays, there was not a significant effect. The reason given was that as w increased the degree of interference of previous over succeeding drops dampened the direct contact of these ones with the hot surface. Similar conclusions were obtained in other studies[11,12] where the boundary between dilute and dense sprays was specified at $w = 2 \, \text{L/m}^2 \, \text{s}$. In addition to the physical interference, the authors[12] argued that as the spray density increases, the local surface temperature does not fully recover before another drop impacts at the same point, diminishing its heat-extraction capability. They claimed also that in dense mists the droplet velocity had a relatively minor effect on the heat transfer, because, although the increase in velocity may increase droplet deformation during impact, it may simultaneously decrease the time duration of the interaction, resulting in a zero net effect;[12] the highest w involved in the study was approximately 8 L/m² s.

Sozbir *et a*l.[12] also indicated that as the droplets impact the surface with more momentum and the water-mass flux increases, the Leidenfrost temperature (*i.e.*, temperature associated with minimum heat flux on the boiling curve) increases. Above this temperature, the superheat is sufficient to establish the film-boiling regime, while below this temperature, intermittent liquid-solid contact gives rise to transition boiling. The dynamics of the wetting/dewetting process is thus determined by a balance between liquid evaporation (pushing toward film boiling) and liquid feeding to the surface (pushing toward transition boiling). Buyevich and Mankevich[13] proposed a model to calculate the critical normal velocity of a single drop, which defines if the impinging droplet is either captured by the surface and ultimately evaporated or almost elastically thrown without removing heat. Buyevich and Mankevich indicated that the critical velocity is a function of the temperature difference between the surface and the liquid, and, therefore, for a constant droplet velocity, the dynamic Leidenfrost temperature corresponds to the surface temperature at which droplet capture goes to zero. The angle of the droplet trajectory with respect to a hot surface also affects the Leidenfrost temperature.[14] Small impinging angles (<45 deg) reduce the Leidenfrost temperature because a large tangential velocity decreases the chance of physical contact between the drop and the surface, and under these conditions the gas boundary layer is likely to be important.[14]

Mathematical-model studies have also been done to describe the velocity and trajectory of drops in mist jets.[15–17] Hatta *et al.*[15,16] developed a two-dimensional (2-D) transient Eulerian–Langrangian model to describe the motion of air and drops in a nozzle chamber and calculate their velocities at its exit and then, through a perturbation of these nonequilibrium velocities, simulated the two-phase flow fields in the free jet and in the impingement region. Hatta *et al.* considered in their analysis 1- and 10-μm particles, finding that the smaller particles tended to concentrate in the jet boundary and were more susceptible to follow the gas-flow pattern. Also, assuming that the particles rebound completely elastically after impinging the surface, they predicted that the finer particles tended to move close and parallel to the surface, while the 10-μm particles separated conspicuously from the surface. These results led the investigators to conclude that the cooling intensity of mists consisting of smaller water droplets was stronger than those made by larger ones. In recent work, Issa and Yao[17] simulated the rebounding of the drops considering empirical information on the variation of the normal coefficient of restitution as a function of the impinging We_{zs} number and assuming that the tangential coefficient of restitution was equal to one. They found that larger droplets rebound farther away from the surface but kept enough of their momentum to impinge back on it. Additionally, their calculations indicated that the cooling profile depends on the droplet-size distribution of the air mists because this parameter influences the trajectories followed by the droplets; in the study, the air- and water-flow rates considered were low, 1.2 to 2 g/s and 10^{-4} to 0.028 L/s, respectively.

Investigations involving air- and water-flow rates and impact-water fluxes within ranges of practical interest to continuous casting (*i.e.*, 5 to 10 g/s (*i.e.*, 3.9 to 7.8 NL/s), 0.3 to 0.6 L/s, and 2 to 90 L/m^2 s, respectively) have shown that the droplet dynamics persist in having an important influence on impaction heat transfer.[18–21] In a study related to crack-sensitive steels, Jenkins *et al.*[18] defined optimum secondary-cooling conditions for A/W ratios in the range of 20 to 30. Jenkins *et al.* argued that these ratios led to the formation of fine and fast drops impinging the strand surface. Also, according to Jenkins *et al.*, the conditions prevailing below that range produced large drops with small specific surface area and thus poor heat-removing capabilities, while operation above the range resulted in fine drops blown away by air currents and never attaining the hot surface. Bendig *et al.*[19] also identified the importance of the air- and water-flow rates on the rate of heat extraction, reporting that the kinetic energy of the drops is the parameter that controls the rate of heat transfer between a hot surface and a cooling air mist. In recent work aimed at a quantitative understanding of the thermal evolution of thin slabs during continuous casting, the present authors found that the prevailing boiling regime is transition boiling and that the rate of heat extraction for a given water-flow rate increases as the air pressure increases from 200 to 250 kPa.[2,20,21] Through laboratory measurements, it was found that this increase in pressure led to an increase in drop velocity and a decrease in drop size that may have resulted in an increased drop-surface contact.[21]

From the preceding review, it is seen that there is a lack of information on the fluid-dynamic behavior of air-mist jets under conditions of interest to continuous casting, despite its important role in determining the contact dynamics and heat extraction from an impinging surface. Hence, the aim of this investigation was to develop a computational fluid-dynamic (CFD) model for simulating the motion of the water droplets and air emerging as a mist from a nozzle. At the nozzle tip, the model considers droplet velocities estimated from a force balance carried out on droplets of different size (determined experimentally) while traveling along the nozzle pipe; the model also takes into account the core angle of the air-mist jet and allows the release of drops from positions stochastically chosen over the nozzle orifice. The computed drop velocities, water-impact flux patterns, and mist-impact pressure fields were compared with experimental measurements obtaining good agreement. Also, it was found that the impinging-droplet Weber numbers are high over most of the water footprint, suggesting that the droplets establish an intimate contact with the solid surface. However, this may be prevented by drop interference at the surface as a result of their high mean fluxes.

II. EXPERIMENTAL WORK

A. Experimental Setup, Conditions, and Procedures

Figures 1(a) through (c) show the experimental apparatus and arrangements employed for measuring drop velocity and size, water-impact density, and mist-impact pressure, respectively. In the experiments, a Casterjet 1/2-6.5-90 nozzle (Spraying Systems Co., Chicago, IL) was used under the conditions indicated in Table I. In the experiments, the water-flow rate was kept constant, while the A/W ratio was varied by increasing the air-nozzle pressure, p_a. The nozzle studied projects a fanlike air mist with a 90 deg core angle, and it is commonly used at a setback distance of 0.175 m from the slab surface. Because, in two-phase flow nozzles, the flow and pressure of the fluids tend to fluctuate as a result of their mutual interaction and the variation of the compressor pressure, these parameters were monitored by digital meters verifying that the measurements stayed within ±7 pct of the desired values.

1. Drop velocity and drop-size measurements

As shown in Figure 1(a), the local drop velocity was measured using a particle-image velocimetry (PIV) system based on a diode laser (Oxford Lasers, HSI 5000, Oxford Lasers Ltd., Didcot, United Kingdom), which produces an infrared-light sheet for illumination of the flow; an electronic controller to select the number, duration, and separation of the laser pulses and an interface for laser-camera synchronization; a charge-coupled device (CCD) camera with a resolution of 1008 (V) × 1018 (H) pixels (Kodak ES 1.0, Eastman Kodak Co., Rochester, NY); a computer with a frame grabber (PIXCI-D-ES-1.0, EPIX Inc., Buffalo Grove, IL); and software for acquisition and analysis of PIV data (AEA Technology, Visiflow; AEA Technology, Didcot, United Kingdom). Despite our interest being the study of jets oriented horizontally, for convenience in the accommodation of the equipment, the measurement of the velocity and size of the drops was done in mists directed downward, as shown in Figure 1(a). The drop velocities should, however, be comparable to those in a horizontally directed mist because the jet length of interest, given by the setback distance, is short and the velocities of the drops are high. It should be noted that the deflection of a droplet during the time it travels (0.175 m) at an average velocity of 30 m/s in the horizontal direction would be just 165 μm (or 0.054 deg).

As shown in Figure 1(a) for the velocity measurements, the camera and the laser gun were placed at 90 deg angle, and the air mists were photographed in quadruple exposure; this number of shot repetitions was important to avoid confusion in recognizing the trajectory of the drops. Their velocities were evaluated using the manual particle-matching technique implemented in Visiflow. Human recognition of the quadruples was necessary because the complexity of the images caused the automatic-analysis techniques to yield poor-quality results. Because the air-mist jets were symmetric, the photographs were taken just over one half of the long middle plane of the jet (with a field of view of 194.5 × 194.5 mm^2), as illustrated in the schematic by region 1. For capturing drop images in the vicinity of the jet axis, the smaller regions (105.4 × 105.4 mm^2) denoted in Figure 1(a) by region 2 and 3 were also photographed. For each condition
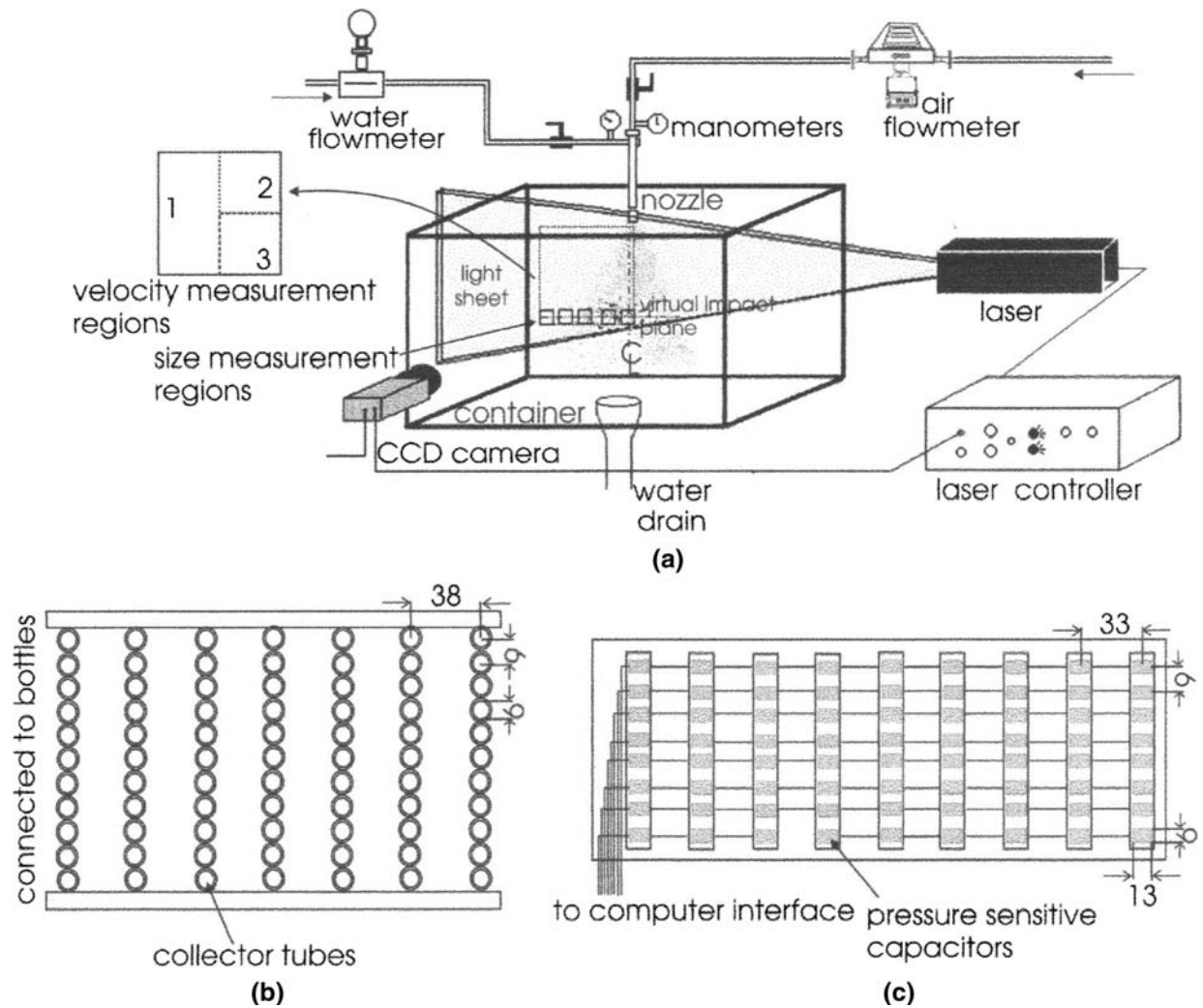
Fig. 1—Schematic diagrams of the experimental apparatus used for the measurement of (a) drop velocity and size, (b) water-impact flux, and (c) air-mist impact pressure. Lengths are in millimeters.

Table I.   Flow Conditions, Fluid Properties, and Nozzle Parameters

Flow Conditions			
Water flow rate, W (L/s)	0.5		
Nozzle air pressure, p_a (kPa)	230	250	290
Air flow rate, A (NL/s (g/s))	5.65 (7.27)	6.93 (8.91)	8.25 (10.61)
A/W ratio	11.3	13.9	16.5
Superficial air velocity at nozzle orifice* (m/s)	65.4	79.31	85.4
Maximum superficial air velocity at nozzle orifice, $U_{z,max}$ (m/s)	81.84	99.44	117.3

Properties of Fluids	
Water density, ρ_d (kg/m^3); Surface tension, σ (N/m); Kinematic viscosity, v (m^2 s^{-1})	998; 7.28×10^{-2}; 2.55×10^{-7}
Air density, ρ (kg/m^3); Viscosity, μ (Pa s)	1.02; 1.5×10^{-5}

Nozzle Parameters	
Half-orifice dimensions, l_x; l_y (m)	0.01; 0.00325
Setback distance, z_s (m)	0.175
Mixing chamber length, z_{mc} (m)	0.25
Jet half angles in x and y directions	45; 10

*Computed from voluminic air flow at 25 °C and 86 kPa considering the effective cross-sectional area

studied, 210 photographs were taken for each of the fields 1 and 3 and 300 of field 2. As discussed in Section IV–A–1, this number of photographs allowed filling with velocity vectors the region of interest of the mist. The separation and duration of the laser pulses for each condition were selected based on preliminary trials.[22]

For the determination of particle size, single-exposure photographs were taken with an exposure time of 6 μs over fields of view of 20 × 20 mm^2. The photographed areas were located at 0, 45, 90, 135, and 180 mm from the nozzle axis and centered around the virtual impact plane, i.e., at 0.175 m from the nozzle orifice, as shown schematically in Figure 1(a). At each position, 40 photographs were taken, and the images were analyzed using Image-Pro Plus (Microimaging Applications Group, Pleasanton, CA) to determine the diameter of the drops captured. The diameter was obtained by averaging the chords measured at 2 deg intervals around the circumference of the drop images. In the experimental arrangement, only drops larger than 25 μm were detected.

2. Water-impact flux and air-mist impact pressure

The local water-flux density, w, was measured at room temperature with the nozzle axis oriented horizontally and directed toward the center of a selected collector in the arrangement shown in Figure 1(b), where each collector was connected to a bottle. While setting the desired water- and air-flow rates, the whole collecting grid remained blocked by a screen, and once the flows stabilized, the screen was removed to initiate the water capture for a period of 40 seconds. The water volume of each bottle was measured by pouring its content into graduated vessels.

To obtain additional information on the behavior of air and air-mist jets impacting on a solid surface, their pressures were measured using dynamic electronic pressure sensors (Tactilus, Sensor Products LLC, Madison, NJ) arranged in a 9 × 8 matrix, as shown in Figure 1(c). The pressure-mapping system was interfaced to a computer for direct reading of the pressures at a programmed sampling time of 0.1 s, over a period of 30 s; a longer test duration did not modify appreciably the time-averaged pressure maps.

III. MATHEMATICAL MODEL

A. System Considered and Assumptions

The system under study was a two-phase jet issuing into stagnant air from the pneumatic nozzle schematically presented in Figure 2(a). The jets were unconfined, and to compare the calculations against the experimental measurements, two situations were considered: nonimpinging and impinging jets. As shown in Figure 2(a), the air fed to the pneumatic nozzles enters axially, while the water does it perpendicularly. After traveling along the mixing chamber, both phases exhaust through a flanged orifice with the half dimensions, $l_x \times l_y$, given in Table I. As illustrated in Figure 2(a) and given in the Table I with other
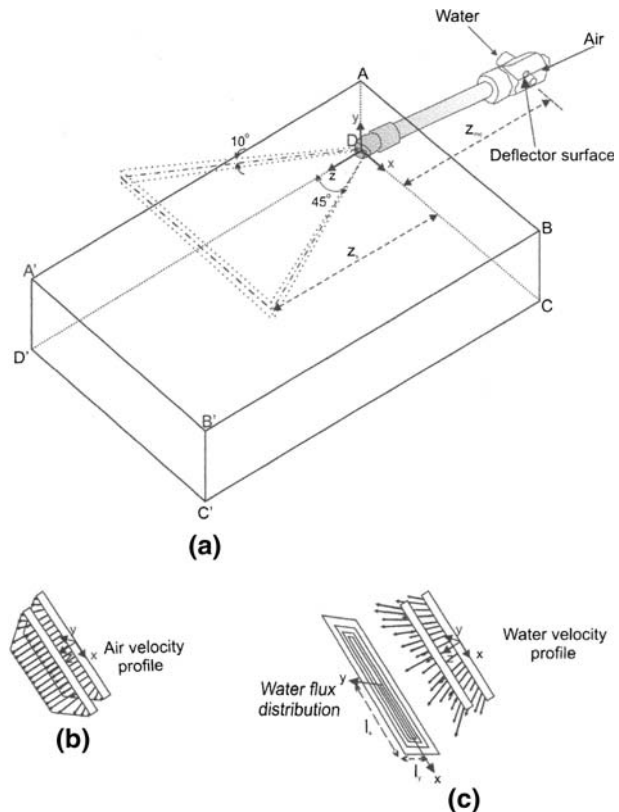

Fig. 2—Schematics of (a) system considered and computational domain, (b) air-velocity profile, and (c) water-velocity profile and flux distribution assumed at nozzle orifice.

parameters, the half angles covered by the drop trajectories were 45 and 10 deg across the x and y directions, respectively. Thus, based on the jet geometry, finite dimensions of the orifice, and the high flow rates of both fluids, it was considered appropriate to treat the problem in three-dimensional (3-D) rectangular coordinates. Because the visual observations of the jets and measurements of the impact footprints indicated double symmetry, over the x–z and y–z planes shown in Figure 2(a), the computational domain included just one quarter of the physical domain. Also, the conditions studied experimentally involved stable water and air-flow rates, and, hence, it was assumed that on a time-averaged basis, the flow characteristics of the two-phase jets could be simulated through a steady-state model.

Because of the scarce information regarding the discharge and flow mode of the water and air emerging from pneumatic nozzles, visualizations of the two-phase jets were carried out, as shown in Figures 3(a) through (c). The photographs show that over the whole jet, the air makes the continuum medium, while the water constitutes the discrete one; the physical properties of both fluids are listed in Table I. As shown in Figure 3(b), the discrete phase appears in the immediate vicinity of the orifice, suggesting, according to Figure 2(a), that as the water stream splashes on the deflector surface and is sheared by the air, it becomes atomized. Then, the drops are propelled by the aerodynamic drag toward the nozzle exit.
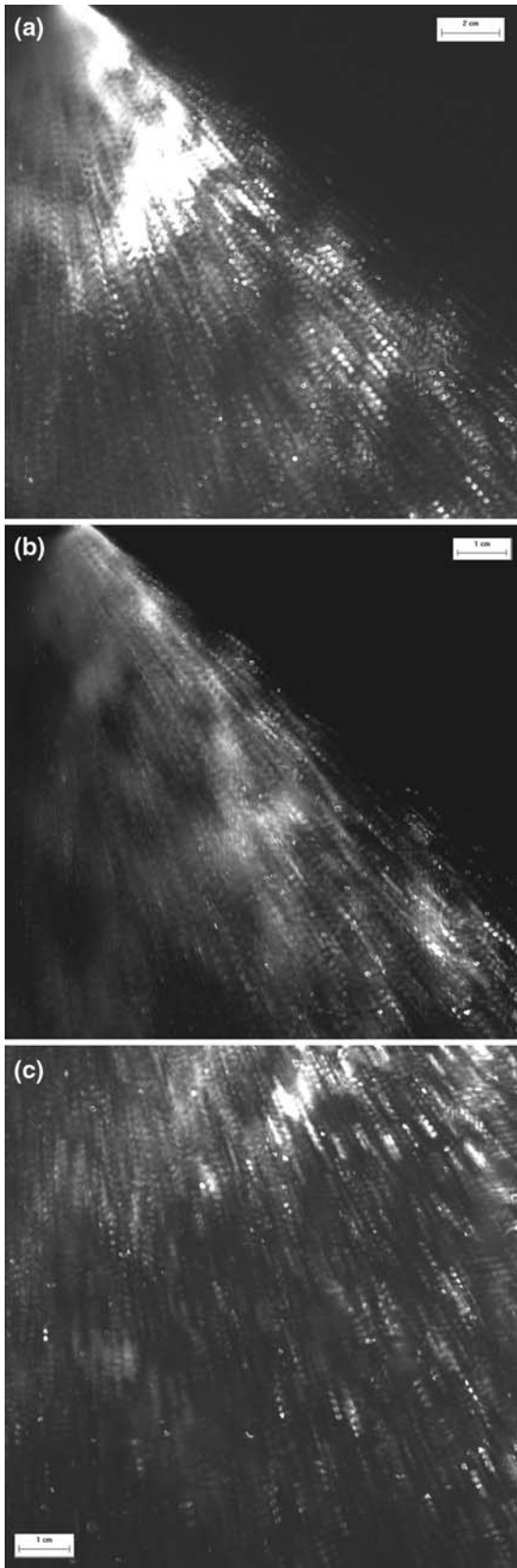
Fig. 3—Quadruple-exposure photographs of drops in air-mist jets generated with $W = 0.5$ L/s and $A = 5.65$ NL/s (7.27 g/s). The photographs correspond to (a) region 1, (b) region 2, and (c) region 3 shown in Fig. 1(a).

This momentum coupling between the two phases must continue in the jet region. On the other hand, since even in the mixing chamber the volume of the drops would make a small fraction of the total volume (approximately 0.081 to 0.057 for the A/W ratios given in Table I), it was assumed reasonable to consider that the drops do not interact among them and, hence, that they do not change in size after forming. Furthermore, due to their small size, the drops were assumed spherical and rigid.

Because the momentum coupling between the air and the drops depends on their relative velocity and size, it was important to obtain an estimate of the size distribution of the drops; this was achieved through the experimental technique described in Section II–A–1. The measurements of the water-drop diameter, over the five sampling regions indicated in that section, are summarized in Figure 4(a) in the form of number-frequency distributions, N_d, for three air-nozzle pressures. Figure 4(a) includes the values of the numerical mean diameter, d_{10}, the volume mean diameter, d_{30}, and the Sauter mean diameter, d_{32}. From the graph, it is seen that the shape and dispersion of the distributions for the different conditions were similar, resulting in similar average quantities. The substantial difference between the number-frequency histograms of the Figure 4(a) resided in the number of drops, N_d, appearing within each size category, and obviously in the total number of drops detected, $N_T = \sum N_d$, at each condition. As explained in a previous article,[21] this behavior must be associated with an increase in the formation of drops finer than 25 μm, particularly after reaching 250 kPa; as indicated in Section II–A–1, these drops were unresolved by the imaging system. The percentage of these finest drops (called ''drops in fog'') for each condition was estimated through a water-mass balance,[21] and the
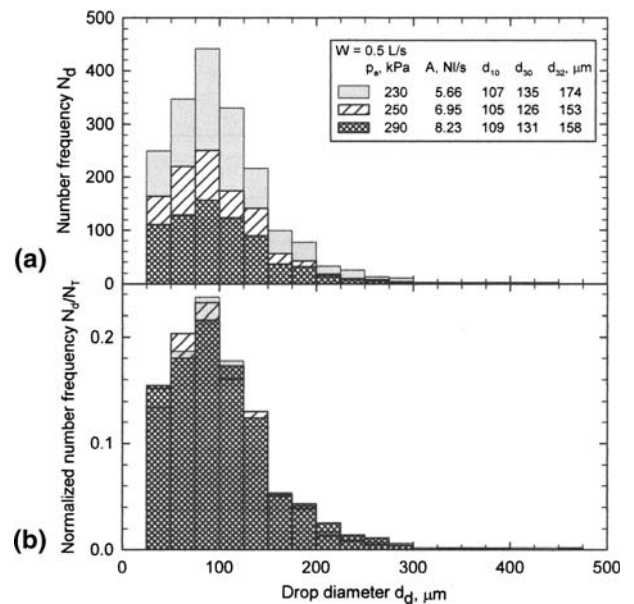

Fig. 4—(a) Droplet-count diameter distributions and (b) normalized droplet-count diameter distributions, measured under different air-nozzle pressure conditions.
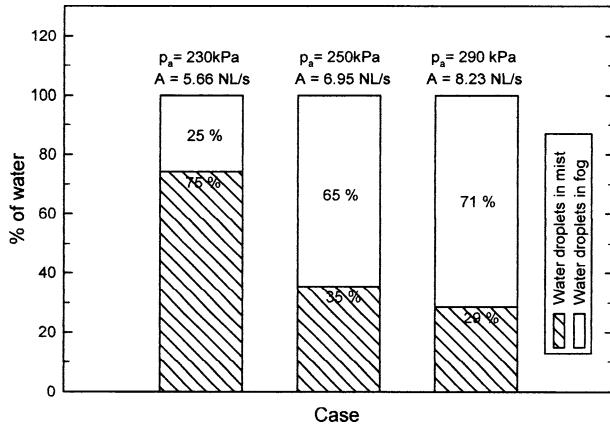
Fig. 5—Estimated percentages of water present as mist ($d_d \geq 25~\mu m$) and as fog ($d_d < 25~\mu m$) in air-water jets generated by a Casterjet 6.5-90 nozzle operating at different air-nozzle pressures and with $W = 0.5$ L/s.

results are shown in Figure 5. As expected, these results are consistent with the decrease in N_T with p_a pointed out by the histograms of Figure 4(a).

Thus, because the distributions in Figure 4(a) do not include an important percentage of the drops that must be present at each pressure condition (*i.e.*, the fraction made by drops $< 25~\mu m$), some supposition had to be made to account for the whole water-flow rate through drops with the measured sizes. In the present model, it was assumed that the number-frequency distributions normalized with respect to the total number of drops, detected at each condition, represented statistically the whole drop population and satisfied the water-flow rate, W, as follows:

$$W = \sum_{k=1}^{n_{p,T}} \dot{\eta}_{d,k} v_{d,k} \qquad [1]$$

where $\dot{\eta}_{d,k}$ and $v_{d,k}$ are the number flow rate of drops (*i.e.*, number of drops/s) and the volume of a drop with diameter, d, exiting from port, k, located on the nozzle orifice, respectively, and $n_{p,T}$ is the total number of ports. The number of ports assigned to each drop-size category, $n_{p,d}$, was prescribed according to the normalized distributions plotted in Figure 4(b) as follows:

$$n_{p,d} = \frac{N_d}{N_T} n_{p,T} \qquad [2]$$

It should be noted that the normalized histograms obtained under the different p_a conditions were very close due to the similarity in the shape of the respective number-frequency distributions. This result was convenient for studying the effect of the air-flow rate on the motion of drops forming the mist; in this work, the term, mist, denotes the two-phase flow containing drops $\geq 25~\mu m$. In addition, parametric calculations were done for drops with $d_d < 25~\mu m$ by assuming similar distributions and considering fog-flow rates corresponding to the proportions given in Figure 5; other details on the treatment of the finest drops are given in Section IV–B–1. The assignment of drops of a given size

category to any port, k, of the orifice is discussed in Section C–2.

Due to the importance of the drop size on the fluid-dynamic behavior of two-phase (air-drops) jets, work is in progress to obtain a better resolution of the image of drops.

For the particles reaching the solid surface, in the case of impinging jets, it was assumed that the particles stick to the surface and were absorbed by it. This assumption may be reasonable because the normal coefficient of restitution could be expected to be very small for the high We_{zs} prevailing under the conditions of interest; however, as it has also been mentioned by Issa and Yao,[17] the tangential coefficient of restitution could not be anticipated to be small.

B. Governing Equations

1. Continuous phase—air

Under the assumptions presented in Section A, the motion of the air phase was described in an Eulerian frame of reference according to the following equations.

Continuity equation:

$$\frac{\partial U_i}{\partial x_i} = 0 \qquad [3]$$

Motion equation:

$$U_i \frac{\partial U_i}{\partial x_i} = -\frac{1}{\rho} \frac{\partial P}{\partial x_i} + (v + v_t) \frac{\partial}{\partial x_j} \left(\frac{\partial U_i}{\partial x_j} + \frac{\partial U_j}{\partial x_i} \right) + S_i \qquad [4]$$

where S_i is the source-term coupling the momentum of the air with that of the drops according to the following expression:

$$S_i = \frac{\pi}{6 \rho v_{cell}} \sum \dot{\eta} \left(\rho_d^o u_i^o (d_d^o)^3 - \rho_d^n u_i^n (d_d^n)^3 \right) \qquad [5]$$

which establishes, according to the particle source in cell model,[23] that the momentum transferred between the air and the drops in a given cell of the fixed Eulerian grid is equal to the change in the momentum of all the drops, $\dot{\eta}$, passing through it over the Langrangian time-step.

The turbulent nature of the air flow was described by the k-ε model for low Reynolds flows of Lam–Bremhorst modified by Yap[24] to reduce the length scale of the turbulence in the viscous sublayer adjacent to the impinging wall, given by the following equation:

$$U_j \frac{\partial k}{\partial x_j} = v_t \left(\frac{\partial U_i}{\partial x_j} + \frac{\partial U_j}{\partial x_i} \right) \frac{\partial U_i}{\partial x_j} - \varepsilon + \frac{\partial}{\partial x_j} \left[\left(v + \frac{v_t}{\sigma_k} \right) \frac{\partial k}{\partial x_j} \right] \qquad [6]$$

and

$$U_j \frac{\partial \varepsilon}{\partial x_j} = f_1 C_1 \frac{\varepsilon}{k} v_t \left(\frac{\partial U_i}{\partial x_j} + \frac{\partial U_j}{\partial x_i} \right) \frac{\partial U_i}{\partial x_j} - f_2 C_2 \frac{\varepsilon^2}{k}$$
$$+ \frac{\partial}{\partial x_j} \left[\left(v + \frac{v_t}{\sigma_\varepsilon} \right) \frac{\partial \varepsilon}{\partial x_j} \right] \qquad [7]$$

where the turbulent-kinematic viscosity is defined as follows:

Table II. Auxiliary Equations

Constants and Functions Involved in the Turbulence Model

$C_1 = 1.44$; $C_2 = 1.92$; $C_d = 0.09$; $\sigma_k = 1.0$; $\sigma_\varepsilon = 1.3$

$f_\mu = (1 - \exp(-0.0165\mathrm{Re}_{z'}))^2 \left(1 + \frac{20.5}{\mathrm{Re}_t}\right)$; $f_1 = 1 + \left(\frac{0.05}{f_\mu}\right)^3$;

$f_2 = 1 - \exp(-\mathrm{Re}_t^2)$

where

$\mathrm{Re}_{z'} = \frac{\sqrt{k}z'}{v}$; $\mathrm{Re}_t = \frac{k^2}{v\varepsilon}$

Drag Coefficient Expressions

Stoke's law region: $\mathrm{Re}_d < 2$ $C_D = 24/\mathrm{Re}_d$
Intermediate region: $2 \leq \mathrm{Re}_d \leq 500$ $C_D = 10/\sqrt{\mathrm{Re}_d}$
Newton's law region: $500 \leq \mathrm{Re}_d \leq 2 \times 10^5$ $C_D = 0.44$
where
$\mathrm{Re}_d = \frac{d_d|U_i - u_i|}{v}$

Coefficients in Eqs. [14] through [16]

$a = \beta/\alpha$; $b = U_z$; $\alpha_1 = 18v\rho/(d_d^2\rho_d)$; $\alpha_2 = 7.5(\rho v)^{0.5}/$
$(\rho_d^{0.5}d_d^{3/2})$; $\alpha_3 = 0.33\rho/d_d\rho_d$; $\beta = (\rho_d - \rho)g/\rho_d$;
$\gamma = b - u_z$; $\gamma_o = b - u_{z,o}$

$$v_t = f_\mu C_d \frac{k^2}{\varepsilon} \quad [8]$$

The constants[25] and the f functions[24] appearing in these equations are listed in Table II. Low Reynolds k-ε models have been recommended[26] for jet-impingement flows characterized by strong streamline curvature, pressure gradients, and recirculation zones; the first two characteristics are prevalent in the jets studied in this work. Additionally, it should be mentioned that Wang and Mujumdar[27] analyzed five versions of low Reynolds-number k-ε models, among them the Lam–Bremhorst modified by Yap model, finding a good performance particularly for high $z_s/2l_x$ aspect ratios, as it corresponds to the present case where $z_s/2l_x = 8.8$.

2. Discrete phase–water drops

As mentioned in Section A, in the system of interest, the volume fraction of the drops is small compared to that of the continuous-phase, therefore the motion of the drops was treated by the Lagrangian method. Their motion equation obeying Newton law considered the aerodynamic drag and the gravity force and was expressed as follows:

$$\frac{du_i}{dt} = \frac{3}{4}C_D \frac{\rho}{\rho_d d_d}|U_i - u_i|(U_i - u_i) + \left(1 - \frac{\rho}{\rho_d}\right)g_i \quad [9]$$

where the drag coefficient, C_D, varies with the particle Reynolds number, Re_d, according to the expressions given in Table II. Other aerodynamic forces that could affect the motion of the droplets (namely the pressure gradient, the virtual mass, and the Basset term) were disregarded because they are of the order of the gas-droplet density ratio,[23] which for the present case is 10^{-3}. Additionally, the Saffman lift and the Magnus forces were also neglected because on most of the flow field, the drops are not in a high-shear region of the air flow;[23] this was justified because in the present article,

the motion of the drops in the vicinity of the impact plane was not analyzed in detail.

The trajectory of the drops was computed from the change of their position-vector components with time as follows:

$$\frac{dx_i}{dt} = u_i \quad [10]$$

C. Initial And Boundary Conditions

1. Continuous phase—air

For specifying the motion of the air phase, only boundary conditions are needed. Ambient conditions were imposed in the upstream and lateral boundaries, denoted by ABCD and BCC'B' in Figure 2(a), as follows:

$$P = P_{\mathrm{amb}}; \quad k = \varepsilon = 0 \quad [11]$$

For simulating a nonimpinging jet, the outlet boundary, A'B'C'D', was specified by imposing $P = P_{\mathrm{amb}}$, and as shown in the Figure 2(a), in order to approach these conditions, the lateral and outlet boundaries where located far away from the jet. For the case of a jet impinging on a solid surface located at $z = z_s$, non-penetration and nonslip conditions where specified as follows:

$$U_i = k = \varepsilon = 0 \quad [12]$$

In the planes, ADD'A' and DCC'D', symmetry conditions were imposed as follows:

$$U_j = \frac{\partial U_i}{\partial x_j} = \frac{\partial k}{\partial x_j} = \frac{\partial \varepsilon}{\partial x_j} = 0 \quad [13]$$

where j represents the index of the coordinate direction normal to the respective symmetry plane.

Due to the little knowledge of the discharge conditions of the air at the nozzle tip, the specification of the inlet boundary was the most uncertain. Thus, to determine the condition that best approached the physical situation, the measured impact-pressure distribution of air was compared against calculated values obtained by solving Eqs. [3], [4], [6], [7], and [11] through [13], imposing different air-velocity profiles at the nozzle tip.[28] The best agreement between both profiles was obtained by specifying an air-velocity distribution with the shape shown in Figure 2(b); i.e., along the x-direction, the profile was uniform over the flat empty portion of the flanged orifice, and in the rest, it decreased to zero varying in angle from 0 to 45 deg at the edge; this distribution was held uniform over the whole orifice thickness. Thus, the mathematical expressions for the inlet air-velocity profile were as follows:

for $0 \leq x \leq 0.585\ l_x$, $0 \leq y \leq l_y$ and $z = 0$
$$U_x = U_y = 0; \quad U_z = U_{zo,\mathrm{max}} \quad [14]$$

and

for $0.585\, l_x < x \le l_x$, $0 \le y \le l_y$ and $z = 0$

$$U_x = U_{z,\max}\left(\frac{0.01 - x}{0.00415}\right)\tan(186.9x - 1.093);$$

$$U_y = 0; \quad U_z = U_{z,\max}\left(\frac{0.01 - x}{0.00415}\right) \quad [15]$$

where the angle in the expression for U_x in Eq. [15] is in radians, and the z component of the velocity field satisfies the prescribed air-flow rate.

The measured and computed air-impact pressure profiles are displayed in Figure 6. It can be noted that the magnitudes of the contours agree reasonably well and that their distributions are similar, although the measured values display a smaller expansion of the jet in the y direction.

2. Discrete phase—water drops

For defining the motion of the water-drops phase in the air-mist jet, only initial conditions are needed. Thus, based on the assumptions presented in Section A, two steps had to be taken. The first step was to specify the exit velocities of drops of different size, and the second step was to define from what positions they would exit and what water-flux distribution they would have at the nozzle orifice.

To accomplish the first step, it was considered that the drops of different size forming on the deflector surface were individually accelerated from a velocity, $u_{z,o} = 0$, while traveling along the length, z_{mc}, of the mixing chamber shown in Figure 2(a). Thus, for calculating the variation of the drop velocity, u_z, as a function of the z position, Eqs. [9] and [10] were integrated analytically together with the expressions for C_D, given in Table II. The following expressions were obtained[28] for the different drag regimes.

Stokes regime:

$$\alpha_1(z - z_o) = u_{z,o} - u_z + (b + a)\ln\left[\frac{\alpha_1 b - \alpha_1 u_{z,o} + \beta}{\alpha_1 b - \alpha_1 u_z + \beta}\right] \quad [16]$$

Intermediate regime:

$$3\sqrt[3]{a}\,\alpha_2(z - z_o) = 2\sqrt{3}(b + a^{2/3})\tan^{-1}\left(\frac{1 - 2(\sqrt{\gamma}/\sqrt[3]{a})}{\sqrt{3}}\right)$$
$$- 2\sqrt{3}(b + a^{2/3})\tan^{-1}\left(\frac{1 - 2(\sqrt{\gamma_o}/\sqrt[3]{a})}{\sqrt{3}}\right)$$
$$+ 2(a^{2/3} - b)\log\left(\frac{\sqrt{\gamma_o} + \sqrt[3]{a}}{\sqrt{\gamma} + \sqrt[3]{a}}\right)$$
$$+ b\log\left(\frac{\gamma_o + a^{2/3} - \sqrt[3]{a}\sqrt{\gamma_o}}{\gamma + a^{2/3} - \sqrt[3]{a}\sqrt{\gamma}}\right)$$
$$+ a^{2/3}\log\left(\frac{\gamma + a^{2/3} - \sqrt[3]{a}\sqrt{\gamma}}{\gamma_o + a^{2/3} - \sqrt[3]{a}\sqrt{\gamma_o}}\right)$$
$$+ 6\sqrt[3]{a}(\sqrt{\gamma} - \sqrt{\gamma_o}) \quad [17]$$

Newton's regime:

$$\alpha_3(z - z_0) = \frac{1}{2}\log\left(\frac{\gamma^2 + a}{\gamma_o^2 + a}\right) - \frac{b\tan^{-1}(\gamma/\sqrt{a})}{\sqrt{a}}$$
$$- \frac{b\tan^{-1}(\gamma_o/\sqrt{a})}{\sqrt{a}} \quad [18]$$

The definitions for the parameters, a, b, α, β, γ, and γ_o, appearing in the equations, are listed in Table II. The numeric solution of the transcendental Eqs. [16] through [18] indicated that drops of all the sizes considered reached their corresponding terminal velocities, $u_{z,t}$, after a short distance from the deflector center.[28] The calculated terminal velocities as a function of drop size are plotted in Figure 7, for p_a equal to 230 and 290 kPa (corresponding to air superficial velocities of 65.4 and 85.4 m/s, respectively). From Figure 7, it is shown that the air superficial velocity has a large effect over the terminal velocity of the finer drops and that, as expected, this decreases with size because of the larger inertia and smaller surface to volume ratio of the larger drops. It can also be observed that after a certain size, which depends on the air superficial velocity, there is an
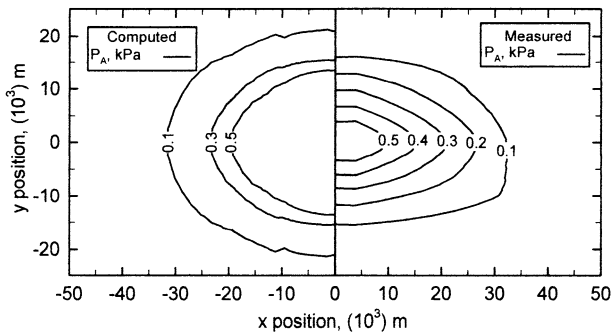

Fig. 6—Computed and measured pressure contours generated by an air jet impacting a solid surface located 0.175 m from the nozzle tip. The air-flow rate was 9.85 NL/s (12.67 g/s) at a nozzle pressure of 194 kPa.
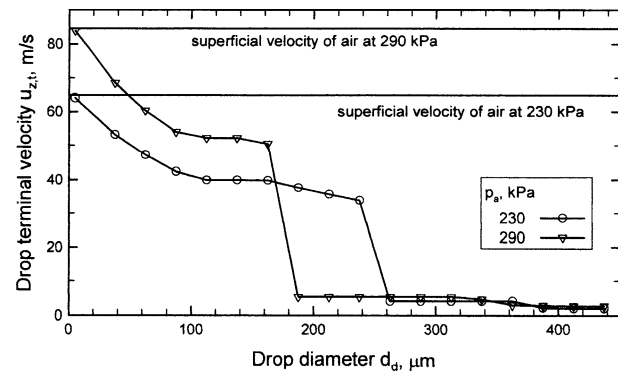

Fig. 7—Terminal drop velocities as a function of size calculated for superficial air velocities based on the effective cross-sectional area of the nozzle orifice. Results for two air-nozzle pressure conditions are shown.

abrupt change in $u_{z,t}$ as the force acting on the particles changes from the intermediate to the Newton-drag regime. For the higher superficial velocity, the transition occurs at a smaller drop size because the momentum-transfer efficiency decreases as the relative air-drop velocity increases. Thus, the initial condition for drops of size, d, exiting through the orifice was prescribed as equal to its corresponding value for $u_{z,t}$.

For accomplishing the second step, the number of ports corresponding to drops of size, d, given by Eq. [2], were stochastically assigned to sites located on the nozzle orifice, assuming equal probability for any site. Additionally, the water-flux distribution through each port was defined through an obelisk distribution,[2] as shown in Figure 2(c). The obelisk pattern was chosen because it has been found[2] to give a good representation of the water footprint at the impact plane, most probably because the drops follow a rectilinear trajectory (Figure 3) during their motion from the nozzle to the impact plane, except very close to it. As suggested also by the observed drop trajectories, according to its assigned position, the drop-velocity angle varied from 0 deg (at $x = 0$) to 45 deg (at $x = l_x$) over the x–z plane and from 0 deg (at $y = 0$) to 10 deg (at $y = l_y$) over the y–z plane. This initialization condition is shown schematically in Figure 2(c).

D. Solution Procedure

Equations [3], [4], [6], and [7] were integrated numerically using the control-volume method of the PHOENICS code,[29] while Eqs. [9] and [10] were solved through its particle-tracking facility. After carrying out mesh-sensitivity analyses, nonuniform meshes of $128 \times 25 \times 93$ and $128 \times 25 \times 107$ control volumes in the (x, y, z) directions were used to solve the impacting- and nonimpacting-jet cases, respectively. The convergence criterion over the domain was set as follows:

$$\sum_{\text{Domain}} \left| E_{\phi P} \right| \leq 10^{-3} \qquad [19]$$

where $E_{\phi P}$ is the residual of the dependent variable, ϕ, at node P. In the model, the drops were released through 6×50 ports (i.e., $N_{p,T} = 300$) distributed uniformly throughout the considered portion of the nozzle orifice, according to the stochastic procedure described in Section III–C–2.

IV. RESULTS AND DISCUSSION

A. Nonimpacting Air-Mist Jets

1. Drop velocities and trajectories
The air stream and the droplet size have a major influence on the velocity at which drops arrive at an impinging surface. Thus, in order to start building a picture of the dynamics of the impact process, it was first necessary to gain insight into the dynamics of the drops as they flew from the nozzle to the impact plane.
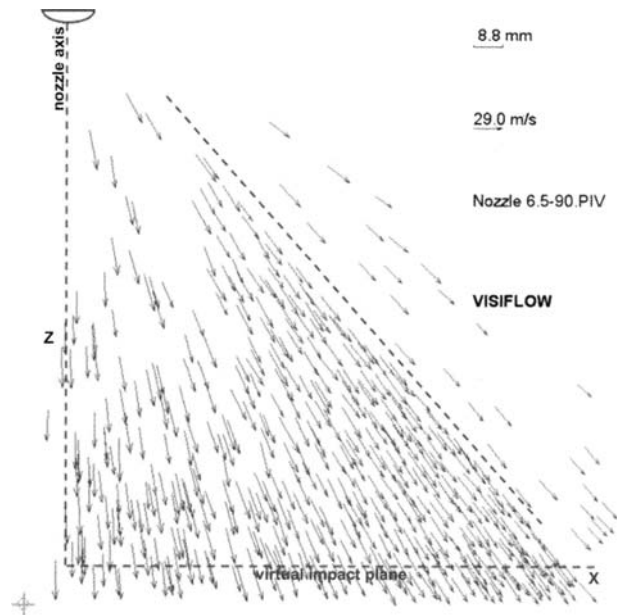

Fig. 8—Experimentally determined vector plot of the velocities of drops travelling in the x–z symmetry plane of air-mist jets generated with $W = 0.5$ L/s and $p_a = 230$ kPa.

Figure 8 shows an experimentally determined vector plot of the velocities of drops moving in a jet. The velocities should correspond to drops with sizes in the range shown in Figure 4; the present technique did not allow associating velocity to size. From Figure 8, it is seen that the drops follow rectilinear trajectories with angles varying from 0 deg at the axis to 45 deg at the jet edge and that the velocities around a given position exhibit a certain degree of dispersion. In using these results for a detailed validation of the model, computed and measured u_x and u_z drop-velocity components were plotted as a function of the x position at three different z distances from the nozzle orifice, as shown in Figure 9. It can be appreciated that the agreement between both results is quite good and that the u_x-velocity component at a given x position decreases as z increases, and the drops interact with the surrounding air, i.e., entraining it to expand the jet. On the other hand, it is interesting to discover that due to the strong drag exerted by the discharged air stream, the u_z component, for drops greater than 25 μm, remains relatively constant with z inside a core region of the jet; only in the jet periphery u_z decreases appreciably with the increase in z.

The computed and measured x- and z-velocity components of drops crossing through the virtual impact plane located at z_s ($= 0.175$ m) are shown in Figure 10, for two air-nozzle pressure conditions. Again, the agreement between both types of results is quite good, and the dispersion that both of them show is associated with the randomness at which drops of different size can leave the nozzle and with their different interaction with the air. The greater dispersion of the measured results may arise because drops of any size may depart from any position in the nozzle, different from the assumption made in the model where only drops with a fixed size can
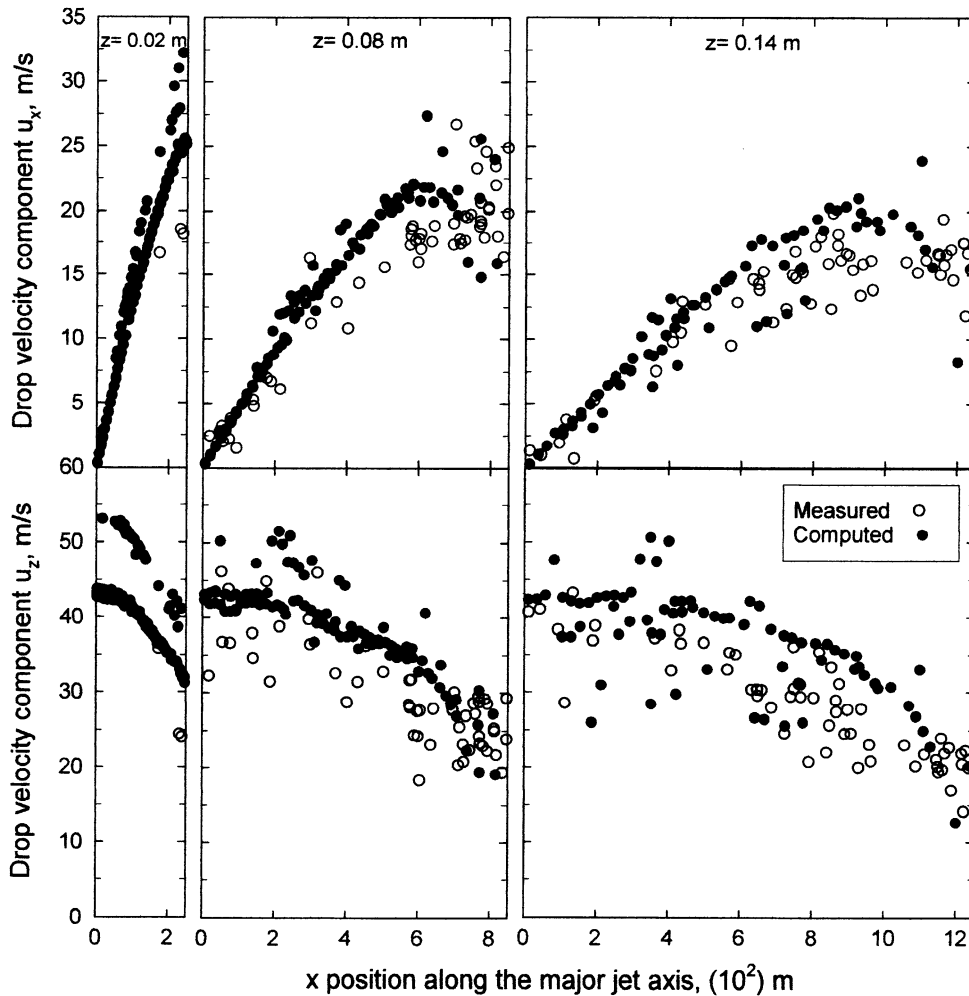
Fig. 9—Comparison between experimental and computed x and z drop-velocity components as a function of the x position at various axial distances from the nozzle orifice and for $W = 0.5$ L/s and $p_a = 230$ kPa. Measurements were made on the x–z symmetry plane of air-mist jets.

depart from a randomly selected port. Additionally, from the plots appearing in Figure 10, it is seen that the u_x velocities are rather similar for both air-pressure conditions and that the difference in the drop-exit velocity, as shown in Figure 7, affects mainly the u_z component. However, the difference caused by the pressure is not large, as can be appreciated particularly when considering the measured u_z values. Hence, based on Figure 5, it would seem that the main effect of the increase in the air-nozzle pressure is a large increase in the proportion of fine drops, *i.e.*, drops <25 μm, that form a fog.

2. Water-impact flux distribution

Local impact water-flux values were evaluated from parameters corresponding to the virtual impact plane using the following expression:

$$w = \frac{1}{A(x,y)} \sum_{k=1}^{n} \dot{\eta}_{d,k} v_{d,k} \qquad [20]$$

where $\dot{\eta}_{d,k}$ and $v_{d,k}$ are, respectively, the number-flow rate and volume of drops following the k trajectories impinging over a small area, $A(x,y)$, of the footprint; in

the present case, areas of 4×1 cm^2 were considered. The measured and calculated water-flux distributions are shown in Figures 11(a) and (b) for $W = 0.5$ L/s and air-nozzle pressures of 230 and 290 kPa, respectively. It can be noticed that the agreement between both results is excellent and that the water-impact flux distribution is unaffected by the air-nozzle pressure. Furthermore, the computed results indicate that the interaction of the drops with the air modifies the initial water-flux distribution, *i.e.*, the obelisk distribution prescribed at the orifice, yielding the typical dog-bone-shaped footprint characteristic of this type of nozzle.

B. Impacting Air-Mist Jets

1. Air-velocity field and drop trajectories

The velocity field of the air in an impacting mist jet is shown in Figure 12, together with the trajectory of a few drops and the impact footprint. From the plot, it is shown that in the neighborhood of the solid surface, the air is deflected mostly along the width of the footprint. On the other hand, for the drop-size range considered, given in Figure 4, it was calculated that all the drops reached the surface, where they lose their momentum by sticking to it
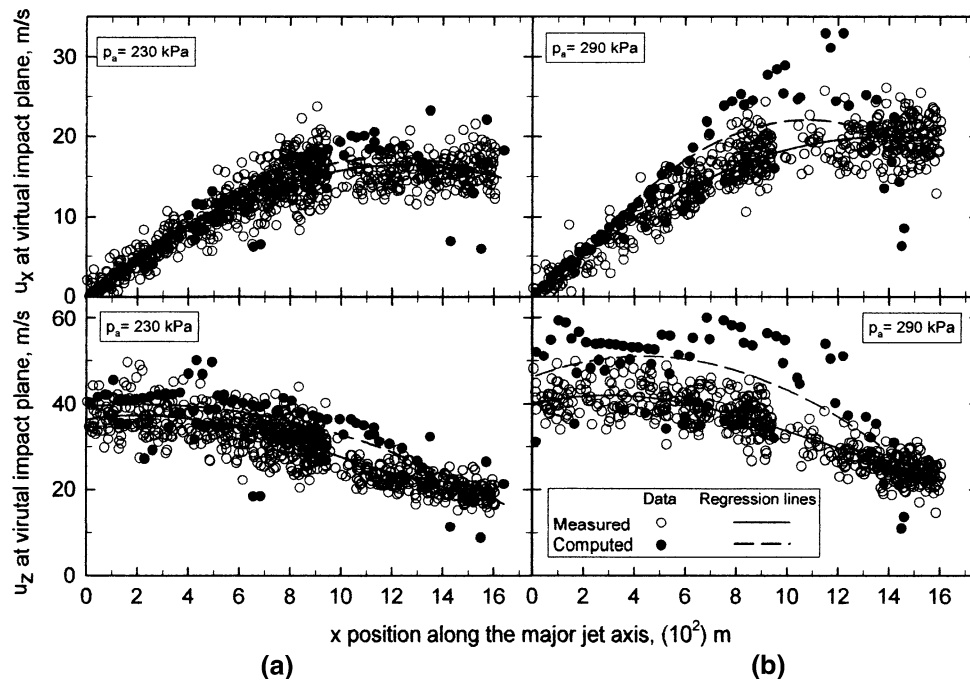
Fig. 10—Comparison between experimental and computed x and z drop-velocity components as a function of the x position at $z = 0.175$ m and for $W = 0.5$ L/min, and (a) $p_a = 230$ kPa and (b) $p_a = 290$ kPa. Measurements were made on the x–z symmetry plane of air-mist jets.
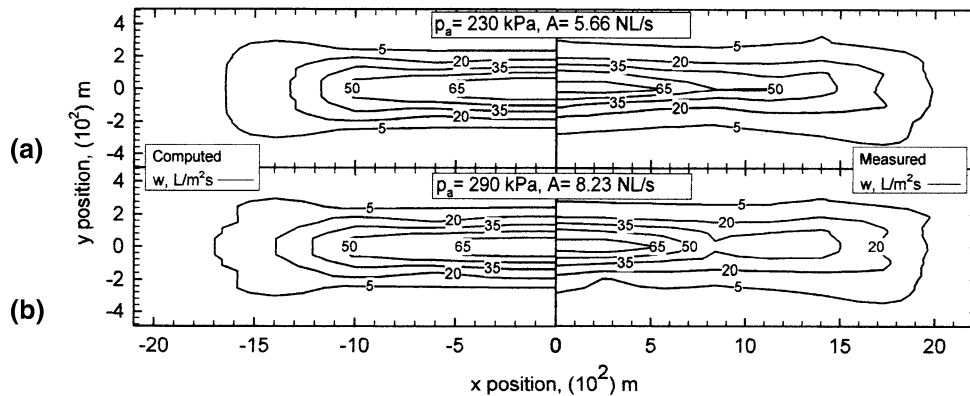

Fig. 11—Computed and measured water-impact flux distributions over a plane located 0.175 m from a Casterjet 6.5–90 nozzle operating with $W = 0.5$ L/s and air-nozzle pressures of (a) 230 kPa and (b) 290 kPa.

and leaving the computational domain, in agreement with the assumption mentioned in Section III–A. Also, Figure 12 indicates that, although the drop trajectories are essentially rectilinear, over most of its flying path, the strong air currents present in the proximity of the solid surface manage to deviate the drops, generating a footprint with the typical dog-bone shape.

Because the results reported in Figure 5 indicated that considerable percentages of the water in the mist are present as fine drops ($d_d < 25$ μm), it was important to investigate their motion in the jet. To do this, a Rosin–Rammler drop-size distribution, as shown in Figure 4(b), was prescribed for these drops, defining eleven size intervals of 2.27 μm each. Similar to the larger drops, the exiting positions of these drops were

assigned randomly over 300 ports, with a flux distribution defined by an obelisk satisfying the estimated water-flow rate for the fog. The flow rates of the water present as fog are given in Table III for each of the conditions considered. Unlike the drops that were detected by the imaging system ($d_d \geq 25$ μm), all of which arrived at the impact plane, the fine drops were susceptible to being blown away by the air currents in the vicinity of the plane, as it is indicated by the trajectories displayed in Figure 13, which includes the trajectories of drops exiting from just a few ports. The present fluid-dynamic model predicts, for all three air pressures considered, that important percentages of the "foggy" drops would not reach the impact plane; the percentages are listed in Table III.

2. Mist-impact pressure

The measured impact-pressure field of a mist generated under an air-nozzle pressure of 290 kPa is shown in Figure 14, together with the calculated value, which was evaluated according to the following equation:

$$p_{zs}(x,y) = \frac{\rho_d}{A(x,y)} \sum_{k=1}^{n} \dot{\eta}_{d,k} v_{d,k} u_{zs,k} + P_{A(x,y)} \qquad [21]$$

where $p_{zs}(x,y)$ is the pressure exerted over an area, A, centered around a position (x,y) located in a plane at $z = z_s$ by the drops ($\geq 25 \ \mu$m for the case of the computations) and the air that impinge upon it. It is noted that the pressure maps agree reasonably well. The greater extension of the calculated pressure field arises from considering only drops that exceed 25 μm and, hence, reach the surface, which is not exactly the case as

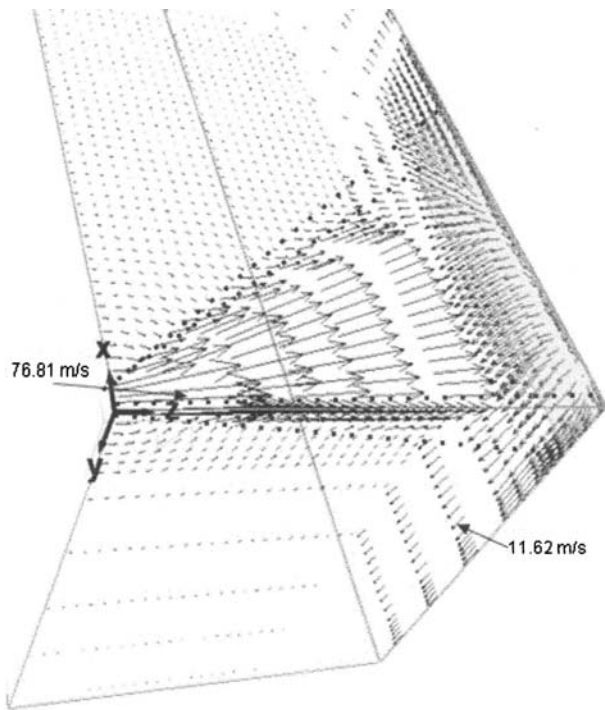discussed in the preceding subsection. Nevertheless, the reasonable agreement between the impact-pressure results lends support to the computed initial-collision velocities, u_{zs}. This is important because this velocity determines the impaction or deformation mode of the droplets and ultimately their contact-surface area and heat-transfer interaction with a hot surface, as it is discussed in Section 3.

3. Drop impaction and arrival onto a solid surface

As mentioned widely in the literature,[5–7,17,30] for single drops or drops in dilute sprays, the relative importance of the drop kinetic energy to its surface energy, as given by the We_{zs} number, is the major factor influencing its impaction dynamics and its heat-extraction effectiveness. For $We_{zs} \leq 1$, the drops would practically deposit on the surface; at $1 < We_{zs} \leq 30$, the drops impact in a
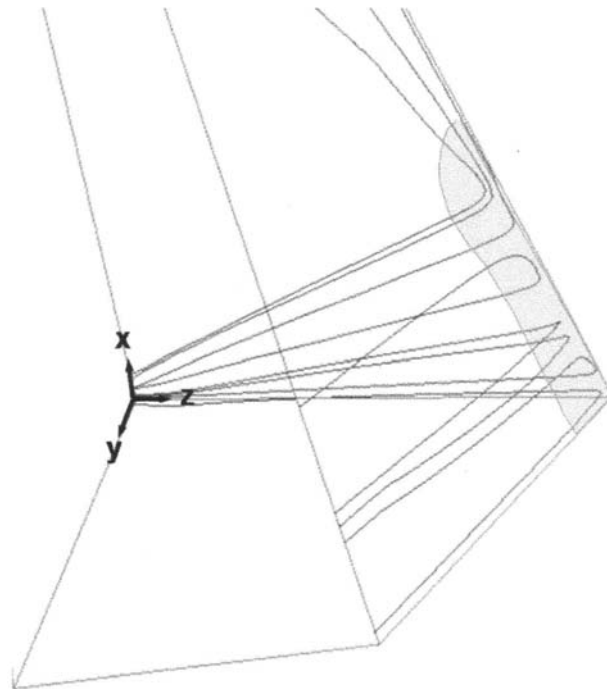

Fig. 12—Air-velocity field computed for an air-mist jet produced by a Casterjet 6.5–90 nozzle operating with $W = 0.5$ L/s and $p_a = 230$ kPa. The dotted lines and the shaded area correspond to drop trajectories and the impact footprint, respectively.

Fig. 13—Computed trajectories of drops $<12.5 \ \mu$m present in an air-mist jet produced by a Casterjet 6.5–90 nozzle operating with $W = 0.5$ L/s and $p_a = 230$ kPa. All the drops not reaching the surface were smaller than 12.5 μm.

Table III. Percentages and Water Flow Rates of the Fog Impinging and Nonimpinging the Surface

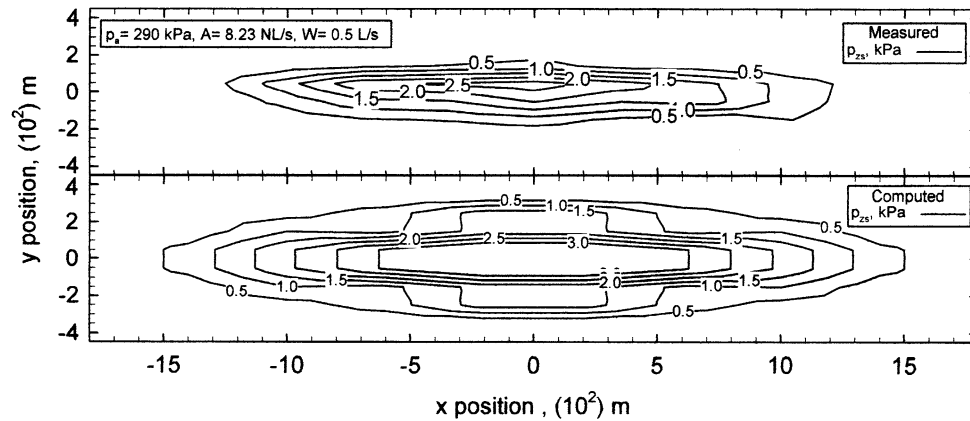|	Nozzle Conditions		
	$W = 0.5$ L/s		
Fog Characteristics	$p_a = 230$ kPa	$p_a = 250$ kPa	$p_a = 290$ kPa
Water flow rate as fog, L/s	0.125	0.325	0.355
Pct of total flow not reaching the surface	11.12	29.24	33.65
Pct of fog not reaching the surface	44.48	44.98	47.40
Water flow rate not reaching the surface, L/s	0.056	0.146	0.168
Water flow rate of fine drops ($\leq 25 \ \mu$m) reaching the surface, L/s	0.069	0.179	0.187
Impact velocity range of fine drops ($\leq 25 \ \mu$m), m/s	0.03 to 15.95	0.09 to 25.43	0.18 to 29.60

Fig. 14—Measured and computed pressure contours generated by a mist-jet impacting on a solid surface located 0.175 m from the orifice of a Casterjet 6.5–90 nozzle, operating under the conditions specified.
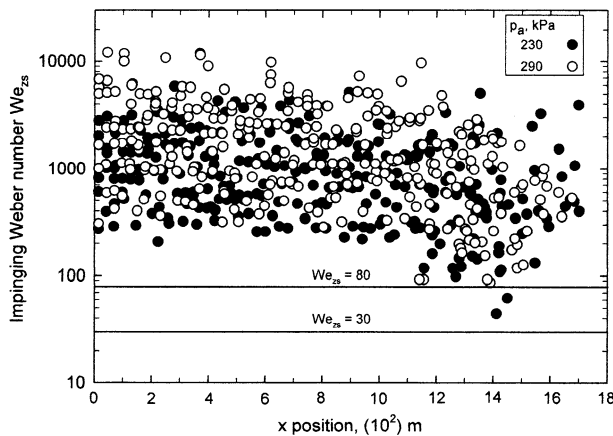

Fig. 15—Predicted normal impinging, We_{zs}, as a function of the x position and for the whole width of the footprint. The results consider drops ≥ 25 μm in mists generated under different air-nozzle pressure conditions.

Fig. 16—Predicted water-flow rates associated with drops <25 μm impinging on a solid surface with different Weber numbers and for different air-nozzle pressure conditions.

nonwetting elastic-rebounding mode; at $30 < We_{zs} \leq 80$, the drops deform plastically, and their rebounding is less intense, and these characteristics are more acute as We_{zs} increases; finally, for $We_{zs} > 80$, the drops spread in a thin film that breaks into several secondary drops.

As mentioned previously, the fluid-dynamic model predicted that all the drops with $d_d \geq 25$ μm reached the impact plane. Thus, Figure 15 shows We_{zs} for the drops emerging from all the orifice ports and impacting at different x positions of the footprint, across its whole width. Figure 15 suggests that practically all the drops in the measured size range would deform into a thin film and break upon impingement. The predictions also indicate that for both air-nozzle pressures considered, the drops ≥ 25 μm posses enough kinetic energy to establish an intimate contact with a solid surface, and therefore, it could be expected that both mists would provide similar heat extraction.

On the other hand, as discussed in Section 1, the air-nozzle pressure conditions have a large effect on the degree of atomization of the liquid inside the nozzle. Thus, it is seen from Figure 5 that the quantity of the
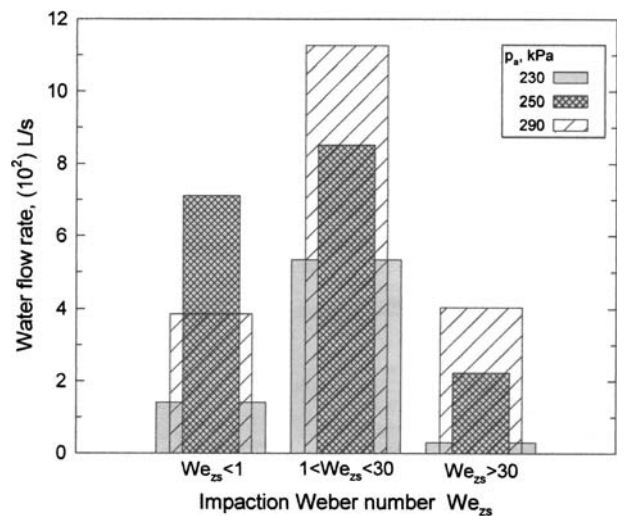
drops <25 μm augmented abruptly when p_a increased from 230 kPa to pressures in the range of 250 to 290 kPa. Hence, although large percentages of the foggy drops are blown away by the air current, important amounts of fine drops are forecasted to reach the surface at the highest pressures, as shown in Table III, i.e., 0.179 and 0.187 L/s vs 0.069 L/s at the lower one. These large flows of drops with large specific surface areas should be responsible for causing the increase in boiling-heat extraction,[2,18] when the air-nozzle pressure increases from 200 to 250 kPa. From Table III, it should be noted also that the fine drops exhibit a wide velocity spectrum, ranging from a few centimeters to several meters per second. The associated computed impaction We_{zs} numbers for the three conditions are shown in Figure 16. From the results, it could be suggested that the appreciable flow rate of foggy drops with $We_{zs} > 30$, generated at the highest air-nozzle pressures (i.e., 250 and 290 kPa), could be responsible for the higher heat-transfer rates measured under these conditions;[2] these

drops could establish an intimate contact with a hot surface. The drops with the smallest We_{zs} numbers also posses the smallest diameter and may evaporate before reaching the surface. Hence, their effect would be a slight lowering of the flow temperature and a slight improvement on the cooling of the surface. The computed results indicated that an important percentage of the flow of these slowly impacting drops posses tangential velocities larger than 10 m/s, suggesting that an intense renewal of drops could take place on the surface; this percentage increases with the increase in p_a. Drops with intermediate We_{zs} numbers would also have a slight influence on the heat extraction because of their reduced contact with the surface.

As found experimentally,[2] the increase in p_a above 250 kPa does not contribute to a further increase in heat extraction, and according to the computed results presented in Table III, it may cause the waste of water. As shown in Table III, the flow rate of water not reaching the surface increases from 0.146 to 0.168 L/s as the pressure augments from 250 to 290 kPa. Thus, the results hint that the atomization conditions should be controlled to produce a high and uniform heat extraction without causing an undue waste of water.

The impact of multiple drops (2 drops) on a solid substrate has been investigated through controlled experiments to determine the shape of the liquid film, the interface between the drops and the shape of the uprising sheet that forms when the fronts of the two spreading drops collide.[30] However, to the best of our knowledge, nothing similar has been reported in the case of interest to secondary cooling where small drops arrive randomly at the substrate in conditions of high water-impact density that make difficult the visual observation of the events happening on the substrate. However, knowing the drop diameter and the water-impact flux can give an approximate picture of how an originally dry solid surface may look after being impinged during a short period of time at the start of spraying. Considering the definitions for the liquid fraction of the mist flow, f ($= w/u_{zs}$), the droplet-number density in the mist, n_d ($= f/(\pi/6) d_d^3$), and the droplet-number flux, $N_d^{\bullet}(= n_d u_{zs})$, the number of drops that impact onto a unit area of the surface during a period Δt can be expressed as follows:

$$N_A = \frac{w}{(\pi/6) d_d^3} \Delta t \qquad [22]$$

The area fraction covered by the deformed drops, S_A, can be expressed as follows:

$$S_A = N_A \left(\frac{\pi}{4} d_o^2\right) \qquad [23]$$

where d_o is the diameter of a spread drop with the form of a cylinder of thickness, b, which according to the experimental results of Toda,[31] depends only on d_d for drop velocities above 5 m/s. Therefore, for constant values of w and d_d, i.e., for constant $N_d^{\bullet}$, the parameters, N_A and S_A, would remain fixed and would be satisfied by any appropriate combination of n_d and u values (i.e., as u increases, n_d must decrease proportionally).

For estimating d_o, Toda[31] measured the thickness of liquid films formed from spherical water drops deformed upon impinging a solid surface and presented a correlation for it as a function of d_d and the kinematic viscosity of the liquid. Then, by assuming volume conservation between the spherical drop and its cylindrically deformed counterpart, Toda was able to calculate the corresponding maximum deformed-drop diameter, d_o. Using this procedure, estimated values of d_o were used to generate Figure 17, which shows computed images of the number of drops that would impact a surface over a period 0.01 ms, together with the area percentage that they would cover once reaching their maximum deformed diameter. The images were generated by considering different d_o and w values and assigning the impinging positions through a random-number generator, assuming equal probability for any site. From the discussion in the preceding paragraph, any of the images in the figure could be generated by mists meeting different concentrations, n_d, and drop velocities, u_{zs}, that maintain $N_d^{\bullet}$ constant, i.e., a dilute mist of high-velocity droplets or a mist made of closely packed slow drops. Then, although both mists would be equivalent in coverage, it could be expected that the first would be preferable from the point of view of heat transfer in the transition-boiling regime, which needs the direct contact of the drops with the surface. High-velocity drops would generate high impact pressure and would deform plastically on the surface, establishing an intimate contact with it.

The impaction modes mentioned at the beginning of the section could be expected when the surface is dry and the impinging drops are far apart so that they do not interact, such as in the situations shown in column (d) of Figure 17. However, in the systems of interest, the impaction dynamics would become more complicated. As suggested by the computed images in the figure, this stems from the reduction in drop size, and the increase in water-impact flux causes that the drops on the surface to no longer behave independently but to start influencing one another. The factors that would distinguish interacting from noninteracting drops at the surface would be w, d_d, and the speed at which the drops are removed from the surface. Considering the derivation of Toda[30] of the time period, τ_d, at which consecutive drops fall over the same position onto the substrate, it has been shown elsewhere[28] that the areas in Figure 17 would be completely covered by a water film after this time has elapsed and if the preceding drops are not removed. The rapid flooding of the surface is consistent with the little increase in heat flux that has been observed to occur after w exceeds a certain value.[2,21] This behavior suggests that the additional water flux would impact on a water layer, which in some places could be separated by a vapor cushion, instead of on the hot surface.

V. SUMMARY AND CONCLUSIONS

This article addresses the fluid dynamics of air-mist jets generated under conditions relevant to the secondary cooling of continuously cast thin slabs. The study
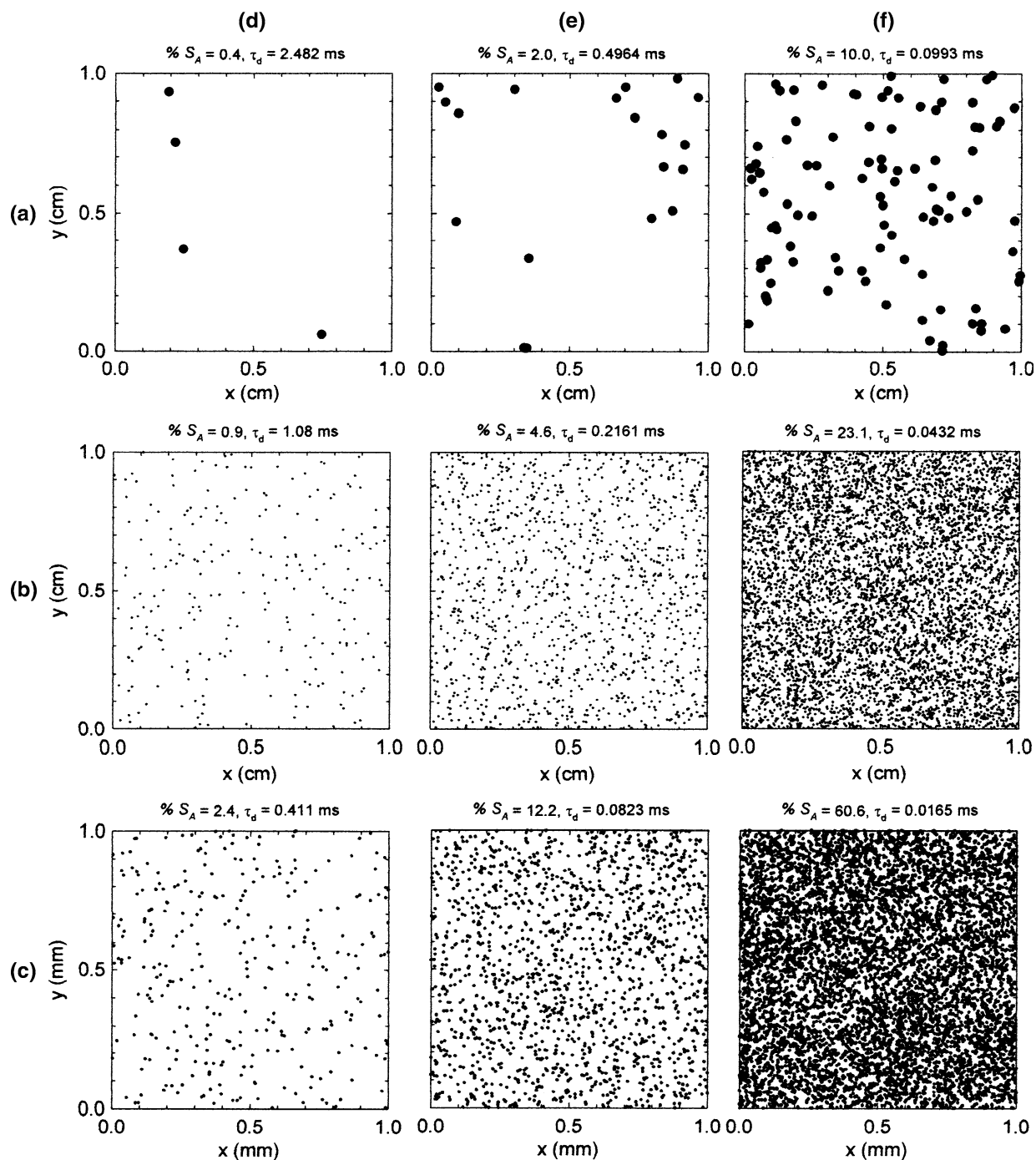
Fig. 17—Computed images of drops arriving at a solid-surface area in a $\Delta t = 0.01$ ms with different d_d values: (*a*) 100 μm, $d_o = 367$ μm; (*b*) 25 μm, $d_o = 69$ μm; and (*c*) 5 μm, $d_o = 10$ μm, and different w values: (*d*) 2, (*e*) 10, and (*f*) 50 L/m^2 s. The fraction area covered by the deformed drops and the time between the arrivals of consecutive drops at the same sites are given for each image. It should be noted that the areas considered in row (c) are of 1×1 mm^2.

involved experimental measurements and computational calculations to analyze the dynamics of nonimpinging and impinging mist jets, under ambient-temperature conditions. The experimental work included laboratory determination of the size, velocity, and trajectories of drops, as well as the water-impact density and pressure of the mists. On the computational side, a CFD simulation was developed based on an Eulerian fluid-flow

turbulence model for the air coupled to a Lagrangian model for the motion of the drops in 3-D and steady state. For setting the model, as it was particularly important to specify the appropriate air-velocity profile at the nozzle orifice, as well as the water-flux distribution, and the velocities (magnitude and angle) and exit positions of drops with the different sizes generated by the nozzle, special attention was given to these aspects.

The model was able to represent very well the parameters measured in the laboratory and to give insight into the phenomena occurring in these systems.

The results indicate that the impaction We_{zs} numbers for drops with $d_d > 25$ μm are sufficiently high (*i.e.*, >80) to expect that upon impaction onto a substrate, they would deform into a thin layer and break, forming secondary drops. However, the computations also indicated that the direct contact of the drops with the surface may be hindered by the interaction of consecutive drops impacting at the same or closely separated sites of the surface. It was suggested that a very short time would be required to flood the surface if preceding drops are not rapidly removed from it. The rapid flooding of the surface is consistent with the little increase in heat flux that has been observed to occur after w exceeds a certain value.[2,21] This situation suggests that the additional water flux would impact onto a water film instead of on the hot surface. As will be reported elsewhere, this behavior undermines the heat-transfer effectiveness of the mist.

The simulation of the motion of drops smaller than 25 μm predicts that important percentages of these drops are blown away by the air currents and never reach the surface; these drops are generally smaller than 12.5 μm. Additionally, it was predicted that particularly at high p_a (*i.e.*, 250 or 290 kPa), large flows of fine drops forming the fog are able to reach the surface with high impaction We_{zs}. These findings suggested that the larger heat fluxes, obtained by increasing the air-nozzle pressure at a given w,[2,21] may be associated with the intimate contact that these fine drops could establish with the surface. Also, their large tangential velocities hint at their active renewal on the surface and, hence, for an intensified heat extraction.

The explanations offered in regard to the fluid-dynamic phenomena responsible for the increase in the boiling-heat extraction with the increase in air-nozzle pressure need a more detailed investigation of the drop-impaction phenomena on both cold and hot solid surfaces and, of course, a better resolution of the drop sizes. Research is underway in our group to gain this deeper understanding.

ACKNOWLEDGMENTS

NOMENCLATURE

A	air flow rate at normal conditions (*i.e.*, 0 °C, 101.3 kPa) (NL/s)
$A(x,y)$	local area in impact plane centered around coordinates, x, y
a, b, α, β, γ, γ_o	coefficients in Eqs. [16] through [18]
C_1, C_2, C_d	constants in the turbulence model
C_D	drag coefficient
d_d, d_o	drop diameter; diameter of deformed drops with cylindrical shape (m)
f	liquid fraction of the mist flow
f_μ, f_1, f_2	functions in turbulence model
g	acceleration due to gravity (m/s^2)
k	turbulence kinetic energy (m^2/s^2)
l_x, l_y	half length and half width, respectively, of nozzle orifice (m)
N_A	number of drops per unit area impacting onto a surface in a time interval Δt (drops/m^2)
n, N, $\dot{N}$	droplet-number density in mist (drops/m^3); number frequency; droplet-number flux (drops/m^2 s)
n_p	port number or number of ports
p_a, p_{zs}	air-nozzle pressure; pressure exerted by the mist on the impinging surface (kPa)
P_A, P	local pressure exerted by the air of an air or mist jet impinging on a surface; pressure (kPa)
$E_{\phi P}$	residual of the discretized equation for the flow variable ϕ (*i.e.*, U_i, k, ε) at node P
Re_d, Re_t, $Re_{z'}$	Reynolds number for drop phase; high turbulence Reynolds numbers
S	source term for momentum-transfer interaction between the drops and the air (m/s^2)
S_A	surface-area fraction covered by deformed drops in a time period (Δt)
Δt, t	time interval; time (s)
u, $u_{z,o}$, $u_{z,t}$	velocity of the discontinuous phase (drops); initial z-velocity component of drop in the mixing chamber; terminal velocity of drops and drop velocity at nozzle orifice (m/s)
U	velocity of the continuous phase (air) (m/s)
v	volume (m^3)
w, W	water-impact density (L/m^2 s); water-flow rate (L/s)
We_{zs}	impinging-droplet Weber number
x, y, z	rectangular coordinates (m)
z_o, z_{mc}, z_s, z'	initial position of drops in mixing chamber; length of mixing chamber; setback distance; distance from solid surface (m)

GREEK

ε	dissipation rate of turbulence kinetic energy (m^2 s^{-3})
v, v_t, v_{eff}	continuous-phase molecular, turbulent, and effective kinematic viscosities (m^2 s^{-1})
ρ, ρ_d	continuous-phase density; discontinuous-phase density (kg m^{-3})

σ	surface tension (N m^{-1})
σ_k, σ_ε,	laminar and turbulent Schmidt numbers for k and ε
$\dot{\eta}$	number-flow rate of drops (s^{-1})
τ_d	period between consecutive drops impinging on the same site (s)

SUBSCRIPTS

amb	ambient conditions, $P = 86$ kPa, $T = 25$ °C
cell	discretization cell
d	drop with diameter (d)
i, j	indexes for coordinate directions
k	index for ports or trajectories
x, y, z	coordinate directions or indexes for vector components
max	maximum
o	orifice
T	total number

SUPERSCRIPTS

o, n	indexes to indicate output and input to control volume

REFERENCES

1. J.K. Brimacombe, P.K. Agarawal, L.A. Baptista, S. Hibbins, and B. Prab-hakar: *Proc. 3rd Steelmaking Conf.*, NOH-BOS Conf., Washington DC, Mar. 23–25, 1980, L.G. Kuhn, R.K. Azar, and G.S. Lucenti, eds., ISS-AIME, Warrendale, PA, 1980, vol. 63, pp. 235–52.
2. J.J. Montes R., A.H. Castillejos E., F.A. Acosta G., and M.A. Herrera G.: *Can. Metall. Q.*, 2008, vol. 47, pp. 187–204.
3. S.G. Hibbins and J.K. Brimacombe: *ISS Trans.*, 1983, vol. 3, pp. 77–89.
4. F.K. McGinnis and J.P. Holman: *Int. J. Heat Mass Transfer*, 1969, vol. 12, pp. 95–108.
5. C.O. Pedersen: *Int. J. Heat Mass Transfer*, 1970, vol. 13, pp. 369–79.
6. K. Araki and A. Moriyama: *Trans. ISIJ*, 1981, vol. 21, pp. 583–90.
7. L.H.J. Wachters and N.A. Westerling: *Chem. Eng. Sci.*, 1966, vol. 21, pp. 1047–56.
8. K. Araki, S.-I. Yoshinobu, Y. Nakatani, and A. Moriyama: *Trans. ISIJ.*, vol. 22, pp. 953–58.
9. H. Xie, S. Koshizuka, and Y. Oka: *Int. J. Numer. Methods Fluids*, 2004, vol. 45, pp. 1009–23.
10. K.J. Choi and S.C. Yao: *Int. J. Heat Mass Transfer*, 1987, vol. 30, pp. 311–18.
11. S. Deb and S.C. Yao: *Int. J. Heat Mass Transfer*, 1989, vol. 32, pp. 2099–2112.
12. N. Sozbir, Y.W. Chang, and S.C. Yao: *Trans. ASME*, 2003, vol. 125, pp. 71–74.
13. Y.A. Buyevich and V.N. Mankevich: *Int. J. Heat Mass Transfer*, 1995, vol. 38, pp. 731–44.
14. S.C. Yao and K.Y. Cai: *Exp. Therm. Fluid Sci.*, 1988, vol. 1, pp. 363–71.
15. N. Hatta, H. Fujimoto, R. Ishii, and J.-I. Kokado: *ISIJ Int.*, 1991, vol. 31, pp. 53–61.
16. N. Hatta, H. Fujimoto, and R. Ishii: *ISIJ Int.*, 1991, vol. 31, pp. 342–49.
17. R.J. Issa and S.C. Yao: *J. Thermophys. Heat Transfer*, 2005, vol. 19, pp. 441–47.
18. M.S. Jenkins, S.R. Story, and R.H. David: *Proc. 19th Australasian Chem. Eng. Conf.*, *CHEMECA 91*, Newcastle, New South Wales, Australia, Sept. 12–20, 1991, Institute of Chemical Engineers, North Melbourne.
19. L. Bendig, M. Raudensky, and J. Horsky: *78th Steelmaking Conf. Proc.*, D.L. Creazzi, C.E. Slater, and K.A. Catanzarite, eds., Nashville, TN, ISS, Warrendale, PA, 1995, vol. 78, pp. 391–98.
20. A.H. Castillejos E., F.A. Acosta G., M.A. García G., R. Santos P., and I. Torres: *Design, Development and Testing of a New Secondary Cooling System for Increasing the Casting Velocity of Thin Slabs, Report for HYLSA, S.A. de C.V.*, DAP, Monterrey, N.L., Mexico, March 6, 2006.
21. A.H. Castillejos E., F.A. Acosta G., M.A. Herrera, I. Hernández C., and E.P. Gutiérrez M.: *ICS Proc. 2005*, Charlotte, NC, AIST, Warrendale, PA, May 8–11, 2005, pp. 881–90.
22. J.I. Minchaca M.: M.Sc. Thesis, CINVESTAV-Unidad Saltillo, Coah., Mexico, Oct. 2007.
23. C.T. Crowe, M.P. Sharma, and D.E. Stock: *J. Fluids Eng.*, 1977, vol. 99, pp. 325–32.
24. C.R. Yap: Ph.D. Dissertation, University of Manchester, Manchester, United Kingdom, 1987.
25. B.E. Launder and D.B. Spalding: *Comput. Math. Appl. Mech. Eng.*, 1974, vol. 3, pp. 269–89.
26. S. Plat, B. Huang, A.S. Mujumdar, and W.J. Douglas: *Annu. Rev. Num. Fluid Mech. Heat Transfer*, 1989, vol. 2, pp. 157–97.
27. S.J. Wang and A.S. Mujumdar: *Appl. Therm. Eng.*, 2005, vol. 25, pp. 31–44.
28. I. Hernández C.: *Ph.D. Progress Reports*, CINVESTAV–Unidad Saltillo, Coah., Mexico, Feb. 2007, 2008.
29. D.B. Spalding: *PHOENICS Software, Version 3.6.1*, CHAM Ltd., London, 2006.
30. I.V. Roisman, B. Prunet-Foch, C. Tropea, and M. Vignes-Adler: *J. Colloid Interface Sci.*, 2002, vol. 256, pp. 396–410.
31. S. Toda: *Heat Transfer—Japanese Res.*, 1974, vol. 3, pp. 1–44.